Robust Predictive Control of Three-Level NPC Back-to-Back Power Converter PMSG Wind Turbine Systems With Revised Predictions

Zhenbin Zhang, *Member, IEEE*, Zhen Li, Marian P. Kazmierkowski, *Life Fellow, IEEE*, José Rodríguez, *Fellow, IEEE*, and Ralph Kennel, *Senior Member, IEEE*

***Abstract*—A direct-drive permanent magnet synchronous generator (PMSG) with a *three-level* neutral-point-clamped back-to-back power converter is an attractive configuration for *high-power* wind energy conversion systems. For such a topology, finite-control-set model-predictive control (FCS-MPC) has emerged as a promising alternative. However, due to its fully model-based concept, variation of system parameters (in particular, the stator and grid filter inductance and rotor permanent-flux linkage) will (seriously) affect the system control performances when using the classical FCS-MPC. In this work, a *robust* FCS-MPC method with *revised predictions* is proposed and validated for such a system. With the proposed solution, *not only* the system robustness against parameter variations is improved, *but also* the control variable ripples are evidently reduced. The proposed method has been implemented with a fully field-programmable-gate-array-based real-time hardware. Its performance improvements in comparison with the conventional solutions are validated with *experimental* data.**

***Index Terms*—Field-programmable gate array (FPGA), finite-control-set predictive torque and power control, nonlinear direct control, robust control, three-level neutral-point-clamped (3L-NPC) back-to-back converter, wind energy system with permanent magnet synchronous generator (PMSG).**

I. Introduction

WIND energy, in particular *high-power* wind energy installation, has steadily increased over the last years. Currently, 7.5-MW systems are available in the market, and numerous research activities aim at 10–12-MW level for offshore applications [1]–[4]. Such a trend requires converter/inverter topologies with more than two voltage levels to handle high power ratings and to meet grid codes with low total harmonic distortions (THDs).

A three-level neutral-point (diode) clamped (3L-NPC) back-to-back converter allows for more than two voltage levels, but the required amount of components is drastically less than, e.g., for five-level topologies. A permanent magnet synchronous generator (PMSG) with a direct-drive structure shows attractive properties [1], [5] (e.g., higher energy density, heavy gear box elimination, and reduced maintenance). Therefore, a direct-drive PMSG wind turbine system with a 3L-NPC back-to-back power converter is a promising configuration for high-power wind energy applications [5]–[7]. Fig. 1 shows a simplified structure of such a system.

Control schemes to deal with such systems, both for the *grid-side converter* (GSC) and *machine-side converter* (MSC), can be divided into two classes when considering whether a modulator is required or not (see, e.g., [8]): 1) modulator-based *linear control methods* and 2) *nonlinear direct control techniques* without a modulator [4], [7], [9]–[11]. Finite-control-set model-predictive control (FCS-MPC), which is one of the well-known nonlinear direct control methods [12], takes the nonlinear and "switching" nature of the power converter into account and combines the control objective optimization and switching state decision processes into one step. A timed-average-based modulation stage is not required therein. Such a technique is capable of dealing with nonlinear dynamics with multiple control objectives and constraints, by using a *flexible* customer designed cost function. It has important advantages, such as straightforward concept, flexible to design, and fast control dynamics. Recently, it has been emerged as a promising alternative for power electronics and drives [12]. However, high computational requirement (in particular for multilevel/multiphase [13], [14] or longer prediction horizon [15] cases) is regarded as one of its drawbacks. Advanced modern digital controllers [e.g., field-programmable gate arrays (FPGAs)] have provided a viable solution for its real-time realization [7], [15].

However, similar to other *model-based control techniques*, control performances using FCS-MPC highly depend on the accuracy of the system model and its parameters [16]. In practice, *unmeasurable* (e.g., flux linkage) and *time-varying* parameters (e.g., resistance and inductance) will inevitably introduce

Manuscript received July 31, 2017; revised November 18, 2017; accepted December 28, 2017. Date of publication January 23, 2018; date of current version August 7, 2018. This work was made possible by the "Qilu Young Scholar" program of Shandong University. The work of J. Rodríguez was supported by Conicyt through Basal Project Grant FB0008 and Fondecyt Grant 1170167 and by the Alexander von Humboldt Society. Recommended for publication by Associate Editor B. Lehman. *(Corresponding author: Zhenbin Zhang.)*

Z. Zhang is with the School of Electrical Engineering, Shandong University, Jinan 250061, China (e-mail: zbz@sdu.edu.cn).

Z. Li is with the School of Physics and Electronics, Shandong Normal University, Jinan 250014, China (e-mail: ZhenLi0901@163.com).

M. Kazmierkowski is with the Institute of Control and Industrial Electronics, Warsaw University of Technology, 00-662 Warszawa, Poland (e-mail: mpk@isep.pw.edu.pl).

J. Rodríguez is with the Facultad de Ingenieria, Universidad Andrés Bello, Santiago 8370146, Chile (e-mail: jose.rodriguez@unab.cl).

R. Kennel is with the Institute for Electrical Drive Systems and Power Electronics, Technische Universität München, 80333 Munich, Germany (e-mail: ralph.kennel@tum.de).

Color versions of one or more of the figures in this paper are available online at http://ieeexplore.ieee.org.

Digital Object Identifier 10.1109/TPEL.2018.2796093

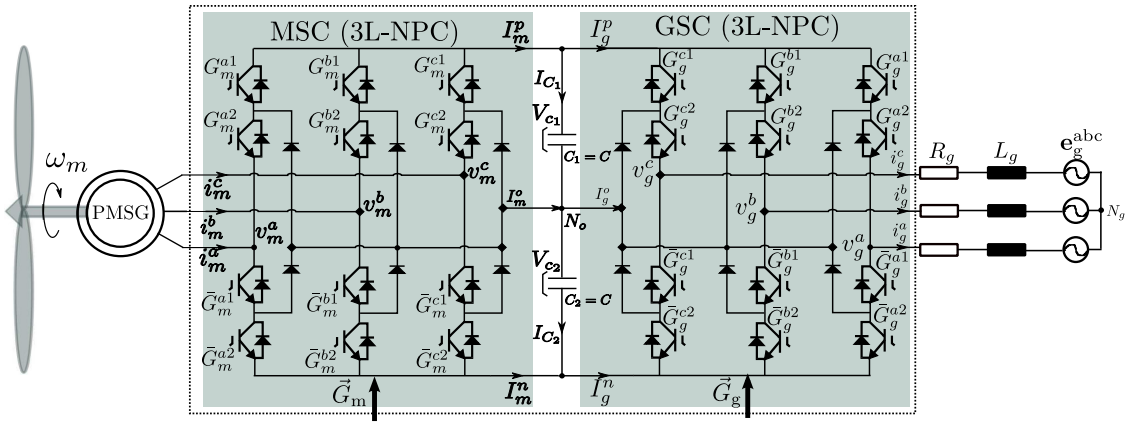

Fig. 1. Simplified electrical circuit of a PMSG wind turbine system with a 3L-NPC back-to-back power converter and an *RL* filter [4], where $\boldsymbol{e}_g^{abc} = (e_g^a,\, e_g^b,\, e_g^c)^\top\,[\mathrm{V}]^3$ is the grid voltage vector, $\boldsymbol{v}_m^{abc} = (v_m^a,\, v_m^b,\, v_m^c\,)^\top\,[\mathrm{V}]^3$ and $\boldsymbol{v}_g^{abc} = (v_g^a,\, v_g^b,\, v_g^c)^\top\,[\mathrm{V}]^3$ are the output voltage vectors of the generator and GSCs, and $\boldsymbol{i}_m^{abc} = (i_m^a,\, i_m^b,\, i_m^c\,)^\top\,[\mathrm{A}]^3$ and $\boldsymbol{i}_g^{abc} = (i_g^a,\, i_g^b,\, i_g^c)^\top\,[\mathrm{A}]^3$ are the generator and grid-side current vectors. $\omega_e(t) = N_p\omega_m\,(t)\,[\mathrm{rad/s}]$ is the electrical frequency of the rotor (rotating with $\omega_m\,[\mathrm{rad/s}]$), N_p [1] is the pole pair number; ψ_{pm} [Wb] is the permanent magnet flux linkage, and θ_e [Wb] is the electrical position of the rotor flux. R_g, R_s [Ω] and L_g, L_s [V.s/A] are the filter and generator stator resistance and inductance, respectively.

mismatch between the actual parameter values and their nominal values used in the controller, which causes performance degradations (e.g., steady-state tracking bias [17] and increased control variable ripples [18]). Particularly, for the system under consideration, i.e., the grid-tied wind turbine system with PMSG, deviations of *both* the inductance (in the generator stator/grid-side filter) *and* permanent magnet flux linkage (of the generator rotor) will considerably affect the system control performances [18]. In the literature, many research efforts, targeting to improve the system robustness against parameter variations, for both the grid- and machine-side control, have been reported. For example, in [19], a Luenberger-observer–sliding-mode-observer-based parameter adaptation method was presented to improve the control robustness against machine stator inductance mismatch. In [20], an online magnet flux linkage estimation approach by using measured speed harmonics was reported to estimate the magnet flux in real time. In [21], an online parameter estimation method using current injection solution was proposed with the same target. In [22], a position offset-based parameter estimation solution for permanent magnet synchronous machines (PMSMs) under variable speed control is proposed. In [23], a grid-side filter inductance estimation method based on the well-known least-squares estimation philosophy was used to improve the system robustness to grid-side inductance variations. In [24], the wavelets were used to analyze transients associated with small disturbances imposed by power converters, and then, the grid impedance was observed using these transients. In general, these aforementioned research studies achieved considerable system performance improvements. However, these methods applied, in general, the "*first-estimation-then-correction*" concept. Hence, an extra state or parameter estimation procedure is inevitably required, which usually requires fast and accurate measurements and will complicate the system control structure. It, hence, increases the system realization efforts and may also reduce its reliability [3], [25]. In [4], the theoretical background and realizations of classical DMPC and switching-table-based direct control strategies of the underlying systems have been comprehensively stated. Their control performances were systematically compared with experimental results. However, robustness-improved approaches were not touched.

In this work, we propose and validate a *robust* FCS-MPC control method with *revised state predictions* for controlling 3L-NPC back-to-back power converters in the direct-drive PMSG wind turbine system. The proposed solution shows *robust* properties against the system inductance and rotor permanent magnet flux linkage variations/uncertainties, with a simple structure and straightforward realizations. It does not require extra fast sampling devices or parameter estimation techniques. Meanwhile, the controller variable ripples are *evidently* reduced, at both the conditions *with* and *without* parameter variations. To conquer the computational efforts required by the proposed robust FCS-MPC solution, a *fully* FPGA-based real-time platform is adopted. The FPGA design process is also detailed. The control performances are thoroughly validated and compared with the classical FCS-MPC scheme, with *experimental* data, at a lab-constructed test bench.

This paper is structured as follows. Section II presents the system modeling and description. In Section III, the control methods of both the classical and the proposed robust FCS-MPC solution are presented. Section IV introduces the FPGA design detail. Section V illustrates the results and their analysis. Finally, Section VI concludes this paper.

II. System Description and Modeling

As depicted in Fig. 1, the GSC and the MSC share a commonly connected dc link of a grid-tied 3L-NPC voltage-source back-to-back power converter. The MSC is the power electronic interface for the machine-side control and the GSC is for the grid-side and dc-link control. The turbine is directly mounted to the generator shaft without a gear box. In the following, such

a system is modeled and described in brief. Note that all quantities $\boldsymbol{x}^{\alpha\beta}$ in the $\alpha\beta$ coordinate and quantities $\boldsymbol{x}^{dq}$ in the dq coordinate are derived using the corresponding quantities $\boldsymbol{x}^{abc}$ in the abc coordinate, invoking (power invariable) Clarke and Park transformation, i.e., for angle $\phi \in \mathbb{R}$ [rad],

$$\boldsymbol{x}^{\alpha\beta} = \underbrace{\sqrt{\frac{2}{3}}\begin{bmatrix} 1 & -\frac{1}{2} & -\frac{1}{2} \\ 0 & \frac{\sqrt{3}}{2} & -\frac{\sqrt{3}}{2} \end{bmatrix}}_{\mathbf{T}_{\mathrm{C}}\ \text{(Clarke transformation)}} \boldsymbol{x}^{abc},$$

$$\boldsymbol{x}^{dq} = \underbrace{\begin{bmatrix} \cos(\phi) & \sin(\phi) \\ -\sin(\phi) & \cos(\phi) \end{bmatrix}}_{\mathbf{T}_{\mathrm{P}}(\phi)\ \text{(Park transformation)}} \boldsymbol{x}^{\alpha\beta}. \tag{1}$$

All models are eventually derived in a discrete-time format applying the forward Euler method of $\frac{d}{dt}x(t) \approx \frac{x_{[k+1]}-x_{[k]}}{T_s}$, to ease the reading of the following controller design sections.

A. Turbine Power, Aerodynamic Torque [4]

The mechanical power extracted by the wind turbine from the wind is governed by (see, e.g., [4] and [7])

$$\begin{aligned} \forall\, k \geq 0:\ P_{t[k]} &= 0.5\rho A \left(v_w(k)\right)^3 C_{p[k]} \\ &= 0.5\rho A \cdot C_{p[k]} \left(\frac{R_t}{\lambda_{[k]}}\right)^3 \times \omega_{m[k]}^3 \geq 0 \end{aligned} \tag{2}$$

where $\rho\,[\mathrm{kg/m^3}]$ is the air density, $A\,[\mathrm{m^2}]$ is the rotor area, R_t [m] is the blade radius, $\lambda_t = \frac{R_t \omega_m}{v_w}$ [1] is the tip speed ratio—depending on the wind speed v_w [m/s], the rotor radius R_t [m], and the generator/machine speed ω_m [rad/s]—$C_p \leq C_{p,\mathrm{Betz}} = 16/27 \approx 0.59$ is the power coefficient of the wind turbine and is a function of the speed tip ratio λ_t and the pitch angle $\beta\,[^\circ]$. For simplicity, it is assumed that the turbine power is transformed without losses to mechanical power into the generator. More detailed discussions can be found in, e.g., [4]. Depending on the wind speed, operation range of a wind turbine system can be divided into five stages [7], [26]. During wind speed stage II, i.e., the wind speed between the cut-in speed and the rated speed, the maximum power can be produced only when the turbine operates at a maximum C_p, i.e., at C_p^{opt}, which depends on an optimum tip speed ratio of λ_t^{opt} (β is kept at zero). A proper "maximum power point tracking" (MPPT) control is required to decide the optimal torque reference $T_{e[k]}^*$ or speed reference ω_m^* command for the inner loop to track. The inner loop of the MSC shall follow either an optimal torque reference $T_{e[k]}^*$ or speed reference ω_m^* command with fast dynamics [4], [7], [26], [27]. In this work, the MPPT control is not the major focus,[1] and we assume that a speed reference ω_m^* fulfilling the MPPT requirement is known for both simulation and experimental verifications.

[1]Interested readers may refer to [26] and [27] for the detailed topics of MPPT control.

B. Generator and Grid-Side State-Space Modeling

Taking the dq-frame stator current $\boldsymbol{i}_m^{dq}(k) = (i_m^d(k), i_m^q(k))^\top$ $[\mathrm{A}]^2$ of a surface mounted permanent magnet generator (SPMSG)[2] and the grid-side power[3] $\boldsymbol{S}(k) = (P(k), Q(k))^\top$ $[\mathrm{VA}]^2$ as the generator and grid-side system states, the discrete state-space model for both the MSC and GSC sides can be expressed as [7]

$$\boldsymbol{x}_y(k+1) = \mathbf{A}_y \cdot \boldsymbol{x}_y(k) + \mathbf{B}_y(k) \cdot \boldsymbol{u}_y(k) + \mathbf{H}_y(k) \tag{3}$$

where $y \in \{m, g\}$, representing the variables for the machine (m) and grid (g) sides, respectively. $\boldsymbol{u}_m(k) = \boldsymbol{v}_m^{dq}(k) = (v_m^d(k), v_m^q(k))^\top$ $[\mathrm{V}]^2$ and $\boldsymbol{u}_g(k) = \boldsymbol{v}_g^{\alpha\beta}(k) = (v_g^\alpha(k), v_g^\beta(k))^\top$ $[\mathrm{V}]^2$ are the input for machine and grid sides, respectively, which are described in Section II-C. $\mathbf{A}_y, \mathbf{B}_y$, and $\mathbf{H}_y$ are the system, input, and feed-through matrices. They are given as follows:

$$\mathbf{A}_m(k) = \begin{bmatrix} 1 - \frac{T_s R_s}{L_s} & T_s\omega_e(k) \\ -T_s\omega_e(k) & 1 - \frac{T_s R_s}{L_s} \end{bmatrix},\ \mathbf{B}_m = \begin{bmatrix} \frac{T_s}{L_s} & 0 \\ 0 & \frac{T_s}{L_s} \end{bmatrix} \tag{4}$$

$$\mathbf{H}_m(k) = \left(0, -\frac{T_s\psi_{\mathrm{pm}}}{L_s}\omega_e(k)\right)^\top \tag{5}$$

$$\mathbf{A}_g = \begin{bmatrix} 1 - \frac{T_s R_g}{L_g} & -T_s\omega_g \\ T_s\omega_g & 1 - \frac{T_s R_g}{L_g} \end{bmatrix} \tag{6}$$

$$\mathbf{B}_g(k) = \frac{-T_s}{L_g}\begin{bmatrix} e_g^\alpha(k) & e_g^\beta(k) \\ e_g^\beta(k) & -e_g^\alpha(k) \end{bmatrix} \tag{7}$$

$$\mathbf{H}_g(k) = \frac{T_s}{L_g}\left(\|\boldsymbol{e}_g^{\alpha\beta}(k)\|^2, 0\right)^\top \tag{8}$$

where ψ_{pm} [V·s] is the permanent magnet flux linkage, T_s [s] is the sampling interval, and ω_g [rad/s] is the grid-side source voltage frequency.

C. 3L NPC Back-to-Back Power Converter

For $y \in \{m, g\}$, $x \in \{a, b, c\}$, and $i \in \{1, 2\}$, the gate signal for the upper insulated-gate bipolar transistors (IGBTs) (see Fig. 1) is introduced as G_y^{xi} and the inverse gate signal for the lower IGBTs as $\bar{G}_y^{xi}$ (complementary to G_y^{xi}; see Fig. 1). We define the switching state u_y^x as

$$u_y^x := \mathcal{G}(G_y^x) = \begin{cases} P, & \text{if } G_y^{x1} = 1 \wedge G_y^{x2} = 1 \\ O, & \text{if } G_y^{x1} = 0 \wedge G_y^{x2} = 1 \\ N, & \text{if } G_y^{x1} = 0 \wedge G_y^{x2} = 0 \end{cases} \tag{9}$$

[2]For which, the equivalent inductance in the dq-axis are equal, i.e., $L_s^d = L_s^q = L_s$ and setting the d-axis $i_m^{d*} := 0$ [A] will lead to maximum torque per ampere control [3].

[3]That is, the power measured from the *point of coupling*, which is [3] $\boldsymbol{S}(k) = ((\boldsymbol{e}_g^{\alpha\beta})^\top(k) \cdot \boldsymbol{i}_g^{\alpha\beta}(k),\ (\boldsymbol{e}_g^{\alpha\beta})^\top(k)[\begin{smallmatrix} 0 & -1 \\ 1 & 0 \end{smallmatrix}]\boldsymbol{i}_g^{\alpha\beta}(k))^\top$, where $\boldsymbol{i}_g^{\alpha\beta}(k) = (i_g^\alpha(k),\ i_g(k)^\beta)^\top$ $[\mathrm{A}]^2$ and $\boldsymbol{e}_g^{\alpha\beta}(k) = (e_g^\alpha(k),\ e_g^\beta(k))^\top$ $[\mathrm{V}]^2$ are the grid-side current and source voltage vectors, respectively.

for phase x. The switching state vector has, therefore, the following form [3]:

$$\boldsymbol{u}_y = (u_y^a\, u_y^b\, u_y^c)^\top \in \mathcal{U}_{27} := \{NNN, NNO, \ldots, PPO, PPP\} \tag{10}$$

of 27 admissible switching states [28]. Hence, for dc-link capacitor voltages V_{c_1} and V_{c_2} (see Fig. 1), the converter phase voltage $\boldsymbol{v}_y^{abc}$ can be obtained as [29]

$$\boldsymbol{v}_y^{abc} = \begin{bmatrix} v_y^a \\ v_y^b \\ v_y^c \end{bmatrix} = (V_{c1} + V_{c2}) \cdot \underbrace{\frac{1}{6}\begin{bmatrix} 2 & -1 & -1 \\ -1 & 2 & -1 \\ -1 & -1 & 2 \end{bmatrix}}_{:=\boldsymbol{T}_{\mathrm{SW}}}$$

$$\boldsymbol{u}_y^{abc} + (V_{c1} - V_{c2}) \cdot \boldsymbol{T}_{\mathrm{SW}} \cdot |\boldsymbol{u}_y^{abc}| \tag{11}$$

where $|\boldsymbol{u}_y^{abc}| = (|u_y^a|\,|u_y^b|\,|u_y^c|)^\top$. The corresponding voltage vectors in $\alpha\beta$ (i.e., $\boldsymbol{v}_{\mathrm{y}}^{\alpha\beta}$) and dq (i.e., $\boldsymbol{v}_y^{dq}$) frames can be obtained invoking the Clark $\mathbf{T}_{\mathrm{C}}$ and Park $\mathbf{T}_{\mathrm{P}}$ transmissions given in (1).

The dc-link voltage $V_d(k)$, when considering the current flow of the converter (see Fig. 1), can be modeled as follows:

$$V_d(k+1) = V_d(k) + \frac{T_s}{C}\Big(I_g(k) - I_m(k)\Big) \tag{12}$$

where $I_g(k) = \boldsymbol{i}_g^{abc}(k) \cdot \boldsymbol{u}_g^{abc\top}(k)$ and $I_m(k) = \boldsymbol{i}_m^{abc}(k) \cdot \boldsymbol{u}_m^{abc\top}(k)$ are the dc-link components of the grid- and load-side currents, respectively. Known from Fig. 1, the capacitor voltage difference $V_{\mathrm{o}} := V_{\mathrm{c1}} - V_{\mathrm{c2}}$ depends on the charging state of the two dc-link capacitors C_1 and C_2 (both $= C$) and will change only when the current I_y^o is drawn from it, i.e., when $\boldsymbol{u}_y$ contains the "O" element [see (9)]. For a given phase current vector $\boldsymbol{i}_y^{abc} := (i_y^a, i_y^b, i_y^c)^\top$, applying the forward Euler approximation yields the discrete-time equation of the dc-link capacitor voltage difference as (see, e.g., [7])

$$V_o(k+1) = V_o(k) + \frac{T_s}{C}\Big(|\boldsymbol{u}_g^{abc}(k)|\boldsymbol{i}_g^{abc\top}(k) - |\boldsymbol{u}_m^{abc}(k)|\boldsymbol{i}_m^{abc\top}(k)\Big). \tag{13}$$

III. Classical and Proposed Control Algorithms

A. Model-Predictive Control and System Requirements

Model-predictive control schemes evaluate a cost function of [3]

$$J(\boldsymbol{u}_{i,j}) = \sum_{h=k}^{k+N-1} \Bigg(\underbrace{\sum_{i=1}^{m} \gamma_{\mathrm{TS_i}} |\mathrm{TS}^*_{i[k+1]} - \mathrm{TS}^p_{i[k+1]}(\boldsymbol{u}_i)|}_{=:J_{\mathrm{TS}}} + \underbrace{\sum_{j=1}^{n} \gamma_{\mathrm{CS_j}} |\mathrm{CS}^*_{j[k+1]} - \mathrm{CS}^p_{j[k+1]}(\boldsymbol{u}_j)|}_{=:J_{\mathrm{CS}}} \Bigg) \tag{14}$$

which represents the control objectives, comprising of general two parts: J_{TS_i} and J_{CS_j} (with weighting factors γ_{TS_i} and γ_{CS_j}, respectively). J_{TS_i} and J_{CS_j} represent subcosts for the ith ($i \in \{1, ..., m\}$) element of the *Target Set* TS (such as tracking of current, voltage, torque, or power with their reference $\mathrm{TS}_{\mathrm{i}}^*$) *and* the jth ($j \in \{1, ..., n\}$) element of the *Constraint Set* CS (such as current/torque or power limitations, switching frequency regulations, and neutral point voltage balancing, etc., with their reference CS_j^*), respectively. $\mathrm{M}_{\mathrm{TS}_i}$ *and* $\mathrm{M}_{\mathrm{CS}_j}$ are abbreviations for the *prediction model for the ith Target TS*$_i$ and the *prediction model for the jth Constraint CS*$_j$, respectively. In this work, a one-step prediction ($h = 1$) is used for the sake of simplicity to demonstrate the effectiveness of the proposed solution.

Back to the system under consideration (depicted in Fig. 1), from the power converter point of view, the control objectives for MSC and GSC are (see, e.g., [3], [7]).

- (co_1) *Torque/current control:* The underlying torque/current controller must be fast and accurate to assure MPPT of the wind turbine system or nominal torque generation for wind speeds above nominal speed. Low torque ripples and low THDs must be guaranteed to reduce stress on the mechanical components.
- (co_2) *Power control:* The GSC assures grid-side power control with fast dynamics, hence, to reduce dc-link fluctuations caused by the changing input wind power. Moreover, a good power quality to fulfill grid codes shall be met.
- (co_3) *Voltage balancing:* At least one side of the back-to-back power converter needs to assure voltage balancing in upper and lower dc-link capacitors (see Fig. 1), i.e.,

$$V_{c1} \stackrel{!}{=} V_{c2} > 0 \implies V_d := V_{c1} + V_{c2} > 0 \tag{15}$$

  is essential (and sufficient) to maintain a constant dc-link voltage and to allow for low-voltage ride-through capabilities [30].
- (co_4) *Switching frequency regulation:* For high-power wind energy applications, low switching frequency so to increase the efficiency and ease the heat-sink design is desirable.

Therefore, to fulfill these control objectives (of $\mathrm{co}_{1,2,3,4}$), the cost functions for the generator (for $y = m$) and grid-side (for $y = g$) control within the FCS-MPC framework can be designed as

$$J_y(\boldsymbol{u}_y) = \boldsymbol{\Gamma}_y \|\boldsymbol{x}_y^* - \boldsymbol{x}_y(k+1)\|^2 + \gamma_y^{\mathrm{sf}} \Delta_{\boldsymbol{u}_y} + \gamma_y^{V_{\mathrm{o}}} \Big(V_{\mathrm{o}}^* - V_{\mathrm{o}}(k+1)\Big)^2, \quad y \in \{m, g\} \tag{16}$$

where $y \in \{m, g\}$, $\boldsymbol{\Gamma}_m = \left[\begin{smallmatrix} \gamma_{i_m^d} & 0 \\ 0 & \gamma_{i_m^q} \end{smallmatrix}\right]$, $\boldsymbol{\Gamma}_g = \left[\begin{smallmatrix} 1 & 0 \\ 0 & 1 \end{smallmatrix}\right]$, and $\gamma_{i_m^q}[1]$, $\gamma_{i_m^d}[1]$, $\gamma_y^{V_{\mathrm{o}}}[1]$ and $\gamma_y^{\mathrm{sf}}, [1]$ are weighting factors. For (16), $\Delta_{\boldsymbol{u}_y}$ is responsible for the switching frequency regulation and is defined as

$$\Delta_{\boldsymbol{u}_y} = \sum_{i=a,b,c} \Big(|u_y^i(k+1) - u_y^i(k)|\Big). \tag{17}$$

Note that, due to the limited scope, the dc-link and speed control loops (we use the same methods as presented in [7]) are not repeated here. In the following, based on the same cost function, both the aspects for the classical and newly proposed robust FCS-MPC methods are discussed.

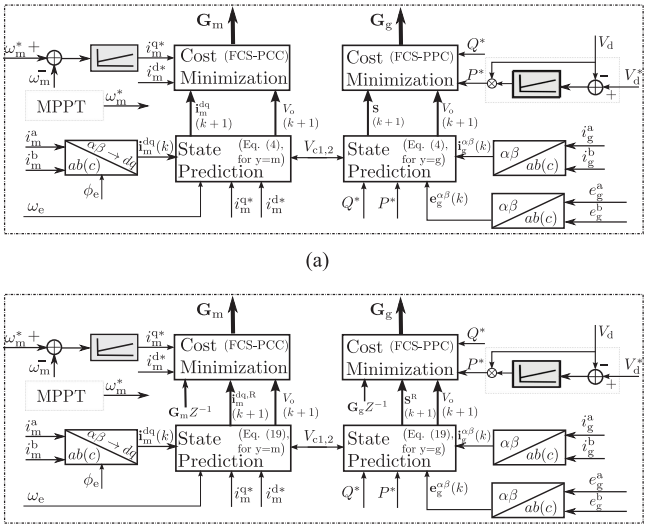

Fig. 2. Structures of (a) the *classical* and (b) the proposed *robust* FCS-MPC for 3L-NPC back-to-back power converter PMSG wind turbine systems.

B. Classical FCS-MPC

For classical FCS-MPC, the predicted currents, power, and neutral point voltage difference are given by (3) and (13), respectively, i.e., *using the original system prediction equations*. Evaluating and minimizing cost function (16) for $\boldsymbol{u}_m, \boldsymbol{u}_g \in \mathcal{U}_{27}$ will yield the optimal gate vectors of $\boldsymbol{G}_y^* := \mathcal{G}^{-1}(\boldsymbol{u}_y^*)$, which will be assigned to the GSC and the MSC, respectively. The overall control structure is shown in Fig. 2(a).

Remark III.1 (Discussion on parameter robustness): Easy to understand, when the system parameters used in the controller mismatch the actual values of the plant, wrong predictions will happen, which will lead to unoptimal switching sequence selections, thereby deteriorating the system control performances. To illustrate such a phenomenon, experimental assessments of using the classical control algorithm were carried out at the lab-constructed test bench, with parameter (resistance, inductance, permanent magnet flux linkage) variation ranges of 50–200% of their nominal values. The parameters are collected in Table II. Results are shown in Figs. 7–9.

As can be clearly seen from Figs. 7–9, with parameter variations, considerable performance degradations are seen: increased system state ripples [see, e.g., Figs. 8(d) and 9(b)] and big tracking bias [see, e.g., Figs. 8(d) and 9(d)] of the control variables.

In the following, we present a new method using revised state predictions with a simple structure to improve system robustness against such parameter variations.

C. Proposed Robust FCS-MPC With Revised Predictions

As aforementioned, with the classical FCS-MPC, *both* the inductance *and* permanent magnet flux linkage variations will affect the system performances considerably. However, their "roles" are different within the system dynamics [see (3)]; the inductance, for both the MSC and GSC sides, is presented in the *system* and *control* matrices $\mathbf{A}_y$ and $\mathbf{B}_y$, while the permanent magnet flux linkage exists only in the *feed-through* matrix $\mathbf{H}_y$. Therefore, we will introduce solutions to improve the robustness against the variations of *inductance* and *permanent magnet flux linkage*, separately, taking their different roles into account.

1) Robustness FCS-MPC Solution Against Inductance Variations: The inductance used in the controller is marked as $\hat{L}_y$ ($y \in \{m, g\}$), while the actual value is L_y, with a modified system state of

$$\boldsymbol{x}_y^{\text{new}}(k) = (1-\lambda)\cdot \boldsymbol{x}_y^p(k) + \lambda \cdot \boldsymbol{x}_y^m(k), \quad \lambda \in (0,1] \tag{18}$$

where $\boldsymbol{x}_y^p$ stands for "predicted" and $\boldsymbol{x}_y^m$ for "measured" values of the system state, λ is a tuning factor (more discussion is presented in Remark III.2). Assuming that a properly working controller exists, the future "predicted" value will approach its "reference," i.e., $\boldsymbol{x}_y^p(k+1) \approx \boldsymbol{x}_y^*(k+1)$. Therefore, invoking (3) and (18), the transfer function in the discrete format between the measurement and the reference becomes

$$\frac{\boldsymbol{x}_y^m(z)}{\boldsymbol{x}_y^*(z)} = \frac{\frac{\hat{L}_y}{L_y}z + (1-\frac{\hat{L}_y}{L_y})\lambda}{\underbrace{\left(z - \left(1-\frac{\hat{L}_y}{L_y}\right)\lambda\right)}_{:=F(z)}}. \tag{19}$$

According to the "bounded-input bounded-output (BIBO)"[4] stability criteria (see, e.g., [31, Ch. 13]), the system is stable, *if and only if* all roots of $F(z) = z - 1 + \lambda\frac{\hat{L}_y}{L_y}$ are inside the unit circle, i.e.,

$$|z| = \left|\left(1-\frac{\hat{L}_y}{L_y}\right)\lambda\right| < 1 \iff$$
$$0 < \frac{\hat{L}_y}{L_y} < \underbrace{1+\frac{1}{\lambda}}_{:=\kappa_{\max}\geq 2}, \text{ where, } 0<\lambda\leq 1\,. \tag{20}$$

Therefore, the safety/stability range of the inductance value $\hat{L}_y$ in the controller is enlarged from the original/conventional solution[5] $(0, 2L_y)$ to $(0, \kappa_{\max}\cdot L_y)$.

Remark III.2 (Discussion on λ): The tunable parameter of λ will add a"weighted average" process to the *measured* and *predicted* values of the system. Therefore, the modified state of

[4]The stability of a sampled closed-loop system, with the discrete-time format of $\frac{C(z)}{R(z)} = \frac{G(z)}{1+GH(z)}$ can be determined by the location of its closed-loop poles in the z-plane, which are the roots of the characteristic equation $1+GH(z)=0$, as follows [31]:

1) *System will be stable*, if the closed-loop poles or the roots of the characteristic equation will lie within the unit circle of $|z|=1$ in the z-plane.
2) *System will be marginally stable*, if a pole or a pair of complex conjugate poles lie(s) on the circle of $|z|=1$.
3) *System will be unstable*, in other cases.

[5]In the original/conventional solution (i.e., the classical FCS-MPC solution), $\lambda = 1$. So, the characteristic function becomes $F(z) = z - 1 + \frac{\hat{L}_y}{L_y}$. Therefore, the BIBO stable requirement is $0 < \frac{\hat{L}_y}{L_y} < 2$.

$\boldsymbol{x}_y^{\text{new}}(k)$, which takes the advantages of this ("weighted average" process), will also add a *smoothing* and *filtering* effect to the system states, for which noises from the measurement channels and sampling delay are inevitable, whenever with or without parameter variations. Therefore, improved control variable quality is expected. The selection of this parameter depends on the quality of analog-to-digital conversion channel quality of the system. In this work, it is obtained in a trail-and-error manner.

So far, the system prediction model has been modified as

$$\boldsymbol{x}_y^{\text{new}}(k+1) = \mathbf{A}_y(k) \cdot \boldsymbol{x}_y^{\text{new}}(k) + \mathbf{B}_y(k) \cdot \boldsymbol{u}_y(k) + \mathbf{H}_y(k). \tag{21}$$

To further reduce the steady-state tracking bias,[6] an integration of the state tracking error (between the previously predicted and the currently measured states) can be added into the revised state prediction model. Considering the drawbacks of a pure integration[7] in practice, the compensation term is processed via a low-pass filter (the parameter α_1 is tuned in a trial-and-error manner) and is expressed as

$$\boldsymbol{x}_y^{\text{comp}}(k) = \frac{1-z^{-1}}{1-\alpha_1 z^{-1}}\left(\boldsymbol{x}_y^*(k) - \boldsymbol{x}_y^m(k)\right) \tag{22}$$

where $\boldsymbol{x}_y^*(k)$ is the reference value of $\boldsymbol{x}_y(k)$. The revised predicted system state [to be evaluated within the cost function (16)], for both the grid and machine sides is therefore

$$\boxed{\boldsymbol{x}_y^R(k+1) = \boldsymbol{x}_y^{\text{new}}(k+1) + \boldsymbol{x}_y^{\text{comp}}(k).} \tag{23}$$

2) Robust FCS-MPC Solution Against Permanent Magnet Flux Linkage Variations: Defining the differences between the controller used and actual *flux* and *inductance* values as $\Delta\psi_{\text{pm}} := \hat{\psi}_{\text{pm}} - \psi_{\text{pm}}$ and $\Delta L_s := \hat{L}_{\text{s}} - L_s$, respectively, taking (3) into account, yields the relationship between the measured q-axis current $i_m^{q,m}$ and the predicted one $i_m^{q,p}$ as

$$i_m^{q,m}(k) = \frac{\hat{L}_s}{L_s} i_m^{q,p}(k) + \frac{\Delta L_s}{L_s} T_s \omega_e(k-1) i_m^d(k-1) + \frac{1}{L_s} T_s \omega_e(k-1) \Delta\psi_{\text{pm}}. \tag{24}$$

In the steady state, for the SPMSG, the d-axis current $i_m^d(k-1) = 0$ and $i_m^q(k) = i_m^q(k-1)$. Therefore, the (*undesired*) difference between the predicted and the measured q-axis current is

$$i_m^{q,\text{error}}(k) := i_m^{q,m}(k) - i_m^{q,p}(k) \approx \frac{T_s \omega_e(k-1)}{L_s} \cdot \Delta\psi_{\text{pm}} \tag{25}$$

i.e., the flux linkage mismatch $\Delta\psi_{\text{pm}}$ proportionally links the current mismatch $i_m^{q,\text{error}}$ at a given speed. Inspired by this, we introduce a solution that *adaptively* compensates the flux linkage used in the q-axis current prediction equation, taking the current

[6]It can be caused by both the model uncertainty and the sampling/calculation delays.

[7]Pure integration will be very sensitive to noises and initial dc bias.

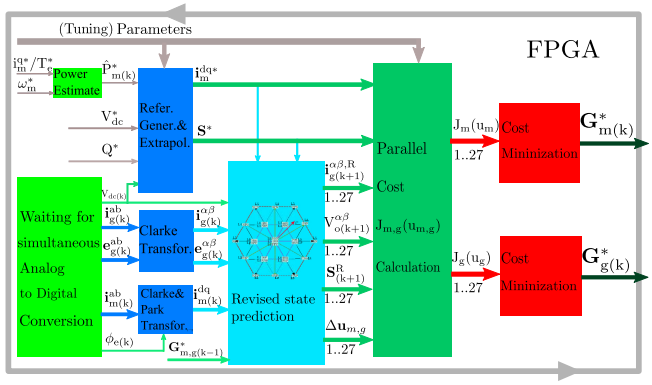

Fig. 3. FPGA design overview and timing information of the proposed *robust* FCS-MPC scheme. Different colors in this figure represent different execution times.

mismatch as the input signal, as follows:

$$\psi_{\text{pm}}^{\text{new}}(k) := \psi_{\text{pm}}(k) + \underbrace{\alpha_2 \cdot \sum \left(i_m^{q,\text{error}}(k)\right)}_{:=\psi_{\text{pm}}^{\text{comp}}(k)} \tag{26}$$

where the parameter α_2 is tuned in a trial-and-error manner. With such a solution, the flux used in the current prediction, i.e., $\psi_{\text{pm}}^{\text{new}}$, will be adaptively updated until the current mismatch of $i_m^{q,\text{error}}$ is eventually eliminated, i.e., the control performance will become immune gamma globulin to flux mismatch.

So far, the proposed robust FCS-MPC solution, to deal with the inductance (of both the machine and grid sides) and flux linkage (of the machine side) variations, is introduced. The overview of the proposed control method is depicted in Fig. 2(b).

For power electronics and electric drive systems, real-time realization and experimental verifications of the underlying control methods are important due to the existing nonmodeled issues. Therefore, in the following, the real-time realization using an FPGA and experimental verification of the proposed solution will be demonstrated.

IV. FPGA Design

FPGAs have become popular for digital controller realizations in the field of power electronics and drives [25]. In this work, both the classical and the proposed *robust* FCS-MPC strategies are implemented on a fully FPGA-based platform (NI-cRIO 9082 system). The strategies have been first verified in Labview-PC environment based on floating point data type and then are modified into fixed point data (all in 18-bit length). After an optimization step using the "single-cycle-timed-loop technique" [7] (to reduce the FPGA hardware resource cost and to improve the execution efficiency), the codes are compiled into "bitfile," which is downloaded into the FPGA-based real-time controller within the same environment. Due to the limited space, only the overview of the FPGA design process for the proposed robust FCS-MPC scheme is shown in Fig. 3. The comparison data of the calculation times and also the resource usage of each method during the FPGA design process are collected in Table I: the proposed *robust* FCS-MPC solution costs slightly

TABLE I
FPGA DESIGN COMPARISON

	Calculation time[8]	Resource usage[9]
Classical FCS-MPC:	273 ticks	58%
Proposed *robust*FCS-MPC:	296 ticks	61%

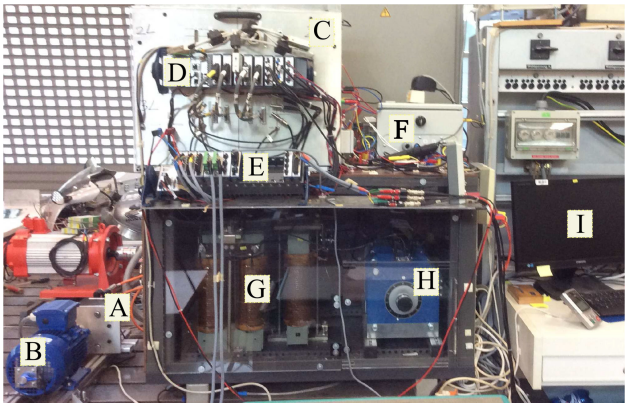

Fig. 4. Lab-constructed test bench for experimental implementation and validation. A: PMSG, B: turbine emulator (ac drive), C: self-constructed 3L-NPC back-to-back power converter, D: NI-CRIO FPGA-based real-time controller, E: real-time chassis for FPGA-based signal-level hardware-in-the-loop test (not used in this work), F: protection devices, G: *RL* filter, H: variac, and I: PC for software development and data logging.

higher FPGA resource usage and longer calculation time than the classical solution, due to the revised prediction model.

V. EXPERIMENTAL RESULTS AND ANALYSIS

In this section, to validate and compare the control performances of both the proposed *robust* (in the following, it is referred to as *Robust* FCS-MPC) and the *classical* FCS-MPC solutions, a grid-tied 3L-NPC back-to-back power converter PMSG prototype was constructed in the laboratory, which is shown in Fig. 4. The differences between the test bench and the topology depicted in Fig. 1 are that a three-phase variac is added between the power line and the grid-side filter to reduce the grid-side phase voltage for safety concerns, and the turbine is emulated using a commercial ac motor drive. The parameters for experiments are collected in Table II. In the following, the effectiveness of the proposed robust FCS-MPC method will be verified. Its experimental performance comparison with the classical FCS-MPC at different testing scenarios, both *with* and *without* parameter variations, will be presented. Results are shown in Figs. 5–9. Corresponding analysis is given in the following sections.

[8]The top clock is 40 MHz; therefore, 1 tick = 1/40 000 000 s = 25 ns.

[9]These data show the FPGA resource usage (solely for the inner control loops). The resource cost for commutation interfaces, data acquisitions, signal saving blocks, etc., was not taken into account. Primary code optimizations are considered to save some resources, for both solutions, during their FPGA realizations.

TABLE II
SYSTEM CONFIGURATION

Parameters	Values
PMSG inductance $L_s^d = L_s^q [H]$	8×10^{-3}
PMSG resistance R_s [Ω]	1.3
PM flux $\psi_{\rm pm}$ [Wb]	0.41
DC capacitance $C_1 = C_2$ [F]	1100×10^{-6}
Grid voltage $\boldsymbol{e}_g^{abc}$ [V]	120
Grid frequency ω_g [rad/s]	100π
Filter resistance R_g [Ω]	1.56e − 3
Filter inductance L_g [H]	16e − 3
Torque/current T_e^n / I_m^n [N·m/A]	8.5/6.3
Rated speed n [r/min]	3000
PMSG pole pairs N_p [1]	3
Sampling time T_s [μs]	50
Weights $\gamma_{i_m^d}, \gamma_{i_m^q}, \gamma_y^{{\rm sf},V_o}$ [1]	0.4, 1, 5%, 2%
Parameters $\alpha_{1,2}$, λ [1]	0.02, 0.0043, 0.61

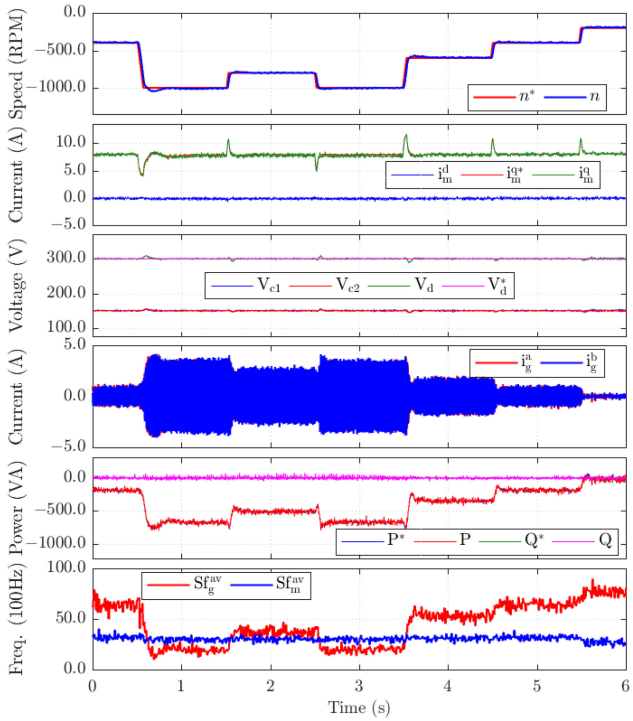

Fig. 5. Experimental data. *Overall* control performance/effectiveness validation of the proposed *robust* FCS-MPC method for grid-tied 3L-NPC back-to-back power converter PMSG wind turbine systems. From up to down are the generator speed, stator currents in the dq frame, dc-link and capacitor voltages, grid-side currents, active and reactive power and their references, and average switching frequency ($\mathrm{Sf}_x^{\rm av}$) of the grid ($x = g$) and machine ($x = m$) sides, respectively.

A. Overall Assessment of the Proposed Robust FCS-MPC

To validate the effectiveness of a control algorithm under test, the overall assessment at wide operation points is very important. In this section, our test scenario is as follows: we assume that the "MPPT speed reference" changes abruptly (with a very steep slope, see top rows in Fig. 5), while the load side torque remains at its 100% of its rated (maximum) value to test the *most harsh* conditions. The dc-link voltage reference V_d^* is set to 300 V, and the reactive power reference is set to be 0 var to

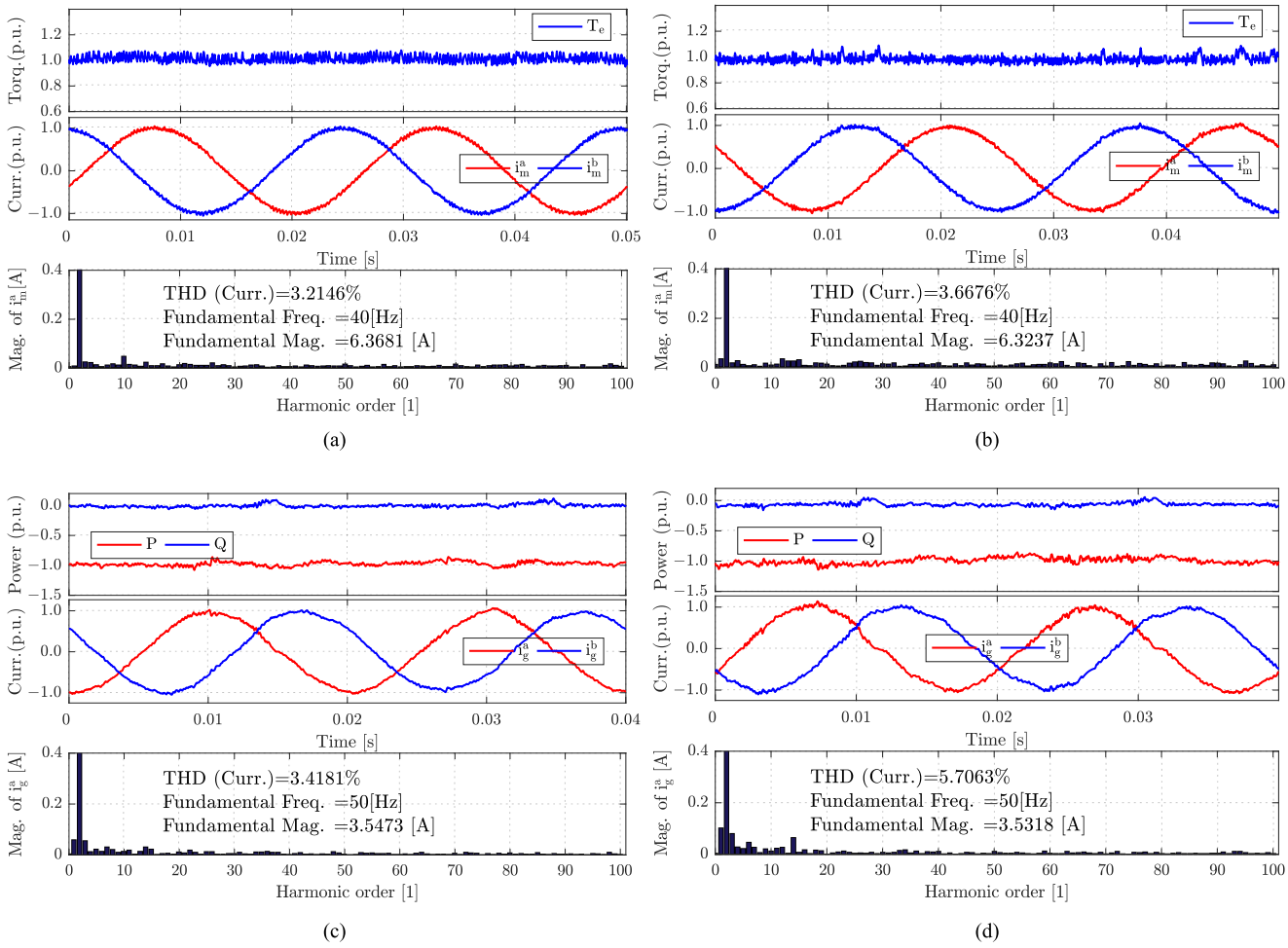

Fig. 6. Experimental data. Control performances comparison at *no parameter variation condition*: (Right) Classical FCS-MPC. (Left) Proposed *robust* FCS-MPC solution. For both figures (a) and (b), from up to down are the electromagnetic torque (base value of 8.5 N·m), stator currents (base value of 6.3 A), and current spectrum, while for figures (c) and (d) from up to down are the grid-side active and reactive power (base value of 700 VA), grid filter current (base value of 3.55 A), and the current spectrum, respectively.

achieve a unity power factor control. The overall control performances for both methods are illustrated in Fig. 5. As can be seen, globally stable, good steady, and transient phase performances are achieved. In detail, smooth speed and current tracking for the machine side and good active and reactive power tracking for the grid side are seen; the dc-link capacitor voltages are well balanced (during both steady and transient phases). However, caused by its inherent characteristic, switching frequency (in particular for the grid side) is not fixed and varies along the operating points.

B. Performance Comparison Between the Classical and Proposed Robust FCS-MPC

To better emphasize and demonstrate the control performance improvement of the proposed solution, in this section, the control performance comparison between the proposed *robust* and classical FCS-MPC solutions, for both the grid and machine sides, is carried out at our laboratory-constructed test bench. Testing conditions are classified into three groups: 1) *normal condition* (i.e., without parameter variations); at conditions of 2) gird and machine stator *inductance variations* and 3) *permanent magnet flux linkage variations*. Under each condition, identical test scenarios for both control methods are configured for fair assessments, e.g., both schemes use the same outer (speed and dc-link voltage) control loops and under the same condition for each testing scenario, etc. Note that the THD values of a current are computed according to the IEEE Standard 1459-2010 [32, Sec. 3.1.2.1]

1) Under Normal Condition: In this test, both the machine- and grid-side controllers use the *nominal parameter values* (of the inductance, the permanent magnet flux linkage, etc.). The results are shown in Fig. 6: smaller torque and power ripples are observed with the proposed solution; when switching to the classical FCS-MPC method under the same condition, the current quality in terms of THD values has increased from 3.21% to 3.67% and 3.4% to 5.7% for machine and grid sides, respectively.

2) At Permanent Magnet Flux Linkage Variations: Permanent magnet flux linkage will vary due to operation condition changes and also age increase of the machine. Robustness against the variation of this parameter is practically very

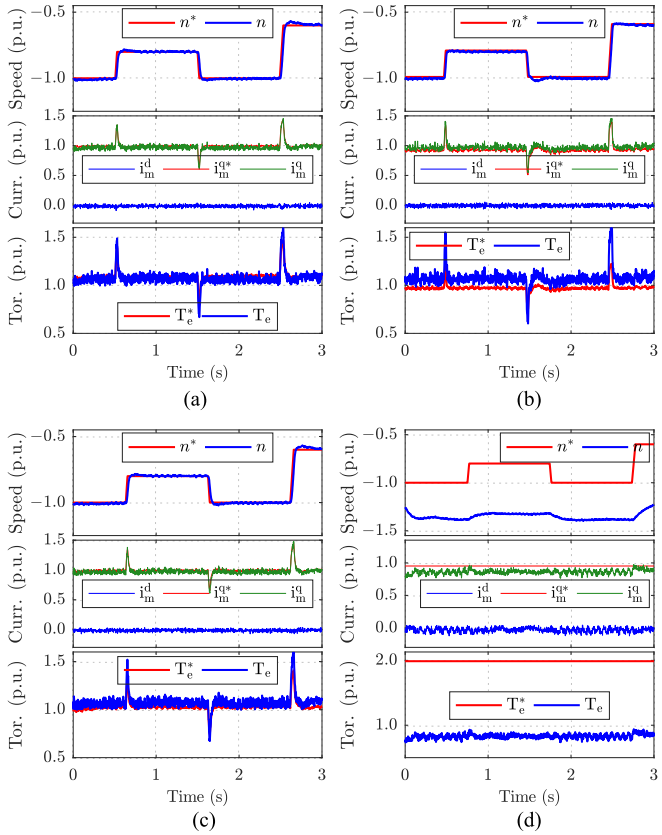

Fig. 7. Experimental data. Performances of the *proposed* and *classical* FCS-MPC methods at 50% [subfigures (a) and (b)] and 200% [subfigures (c) and (d)] of the nominal permanent magnetic flux conditions (ψ_{pm}). For all subfigures, from up to down are the generator speed (base value of 1000 r/min), stator currents (base value of 6.3 A) in the dq frame, and the electromagnetic torque (base value of 8.5 N·m).

desirable. In this section, we tested both methods under the permanent magnet flux linkage variations of 50% to 200% of its nominal values.[10] The results are shown in Fig. 7: at 50% of the nominal permanent magnet flux linkage, although both methods work still stably, increased tracking bias and control variable ripples are seen with the classical solution. However, at 200% of the nominal permanent magnet flux linkage, the classical solution runs into instability, while slightly increased tracking bias is seen with the proposed solution.

3) At Grid and Machine Stator Inductance Variations: The inductance values for the generator and grid-side filter used inside both controllers are varied (to 50% and 200% of its measured values) under same conditions (with same outer loops and during rated turbine torque) to investigate their robustness to inductance variations. Results are collected in Figs. 8 and 9. As can be seen, in both cases, the proposed *robust* FCS-MPC solution outperforms the classical FCS-MPC method in terms of (much) smaller ripples, tracking biases, and also current THDs.

[10]In practice, the value of both grid and PMSM stator inductance will change in a small range, e.g., 10–20%. However, the permanent flux, due to long operation time span and rigid operation conditions, might change in a larger range, e.g., 30–40% or even more. To validate the effectiveness of the proposed solution for all the considered parameter changes (including the permanent flux), we choose a wider range of 50% and more so as to more *sufficiently* draw our conclusion that the proposed solution is effective.

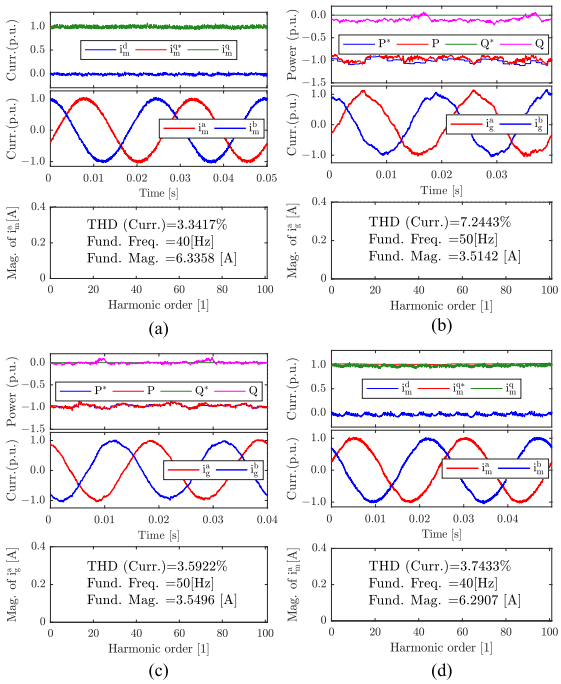

Fig. 8. Experimental data. Performances of the *proposed* [subfigures (a) and (c)] and *classical* [subfigures (b) and (d)] FCS-MPC methods at *50% of the nominal stator and filter inductance condition*. For subfigures (a) and (b), from up to down are the stator currents (base value of 6.3 A) in dq and $ab(c)$ frames and the current spectrum, respectively, while for (c) and (d) from up to down are the grid-side active and reactive power, filter currents, and the current spectrum, respectively.

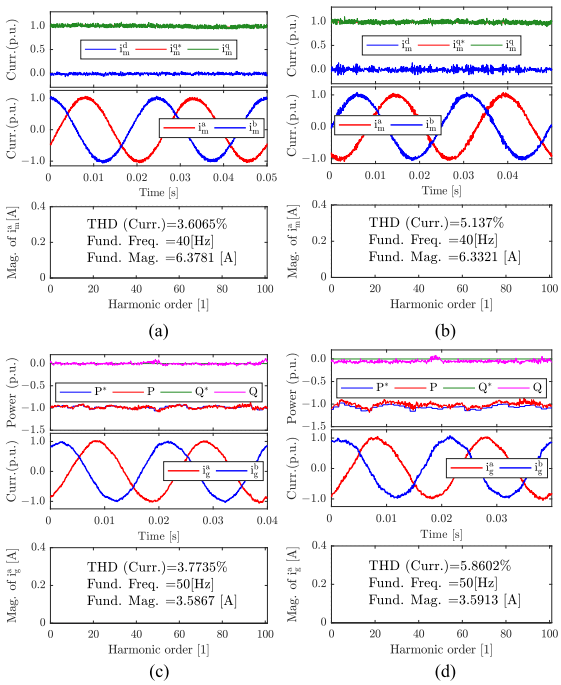

Fig. 9. Experimental data. Performances of the *proposed* [subfigures (a) and (c)] and *classical* [subfigures (b) and (d)] FCS-MPC methods at *200% of the nominal stator and filter inductance condition*. For subfigures (a) and (b), from up to down are the stator currents (base value of 6.3 A) in dq and $ab(c)$ frames and the current spectrum, respectively, while for (c) and (d) from up to down are the grid-side active and reactive power, filter currents, and the current spectrum, respectively.

VI. Conclusion

Wind energy applications, in particular wind energy application system with *high-power rating configuration*, have drawn increasingly much attention, which makes the 3L-NPC back-to-back converter with a direct-drive PMSG configuration an interesting choice. For such a topology, FCS-MPC has emerged as a promising alternative, due to its straightforward concept and flexible design process. However, parameter variations will lead to performance degradations for such fully model-based techniques. To conquer some of these problems, in this work, we have proposed a *robust* FCS-MPC solution with *revised state predictions*. Both the classical and the proposed solution have been realized and tested at a fully FPGA-based platform. The proposed robust FCS-MPC method is characterized by the following features and advantages.

1) It has a simple structure and is easy to implement.
2) It outperforms the classical FCS-MPC solution at different scenarios both with and without parameter variations, as shown by experimental measurements.
3) Only a slightly higher FPGA resource usage is required.
4) Additionally, the proposed solution can be easily extended to other FCS-MPC alternatives (e.g., speed, flux, current control, etc.) with few modifications.

Future work will focus on the extension of the proposed solution to other topologies and systems.

References

[1] F. Blaabjerg and K. Ma, "Future on power electronics for wind turbine systems," *IEEE J. Emerg. Sel. Topics Power Electron.*, vol. 1, no. 3, pp. 139–152, Sep. 2013.

[2] J. M. Carrasco *et al.*, "Power-electronic systems for the grid integration of renewable energy sources: A survey," *IEEE Trans. Ind. Electron.*, vol. 53, no. 4, pp. 1002–1016, Jun. 2006.

[3] Z. Zhang, "On control of grid-tied back-to-back power converters and permanent magnet synchronous generator wind turbine systems," doctoral dissertation, Dept. Electr. Drive Syst. Power Electron., Tech. Univ. München, München, Germany, 2016.

[4] Z. Zhang, F. Wang, J. Wang, J. Rodrguez, and R. Kennel, "Nonlinear direct control for three-level NPC back-to-back converter PMSG wind turbine systems: Experimental assessment with FPGA," *IEEE Trans. Ind. Informat.*, vol. 13, no. 3, pp. 1172–1183, Jun. 2017.

[5] M. Liserre, R. Cardenas, M. Molinas, and J. Rodriguez, "Overview of multi-MW wind turbines and wind parks," *IEEE Trans. Ind. Electron.*, vol. 58, no. 4, pp. 1081–1095, Apr. 2011.

[6] Z. Chen, J. M. Guerrero, and F. Blaabjerg, "A review of the state of the art of power electronics for wind turbines," *IEEE Trans. Power Electron.*, vol. 24, no. 8, pp. 1859–1875, Aug. 2009.

[7] Z. Zhang, C. M. Hackl, and R. Kennel, "Computationally efficient DMPC for three-level NPC back-to-back converters in wind turbine systems with PMSG," *IEEE Trans. Power Electron.*, vol. 32, no. 10, pp. 8018–8034, Oct. 2017.

[8] M. Kazmierkowski, L. Franquelo, J. Rodriguez, M. Perez, and J. Leon, "High-performance motor drives," *IEEE Ind. Electron. Mag.*, vol. 5, no. 3, pp. 6–26, Sep. 2011.

[9] M. Depenbrock, "Direct self-control (DSC) of inverter-fed induction machine," *IEEE Trans. Power Electron.*, vol. 3, no. 4, pp. 420–429, Oct. 1988.

[10] I. Takahashi and T. Noguchi, "A new quick-response and high-efficiency control strategy of an induction motor," *IEEE Trans. Ind. Appl.*, vol. IA-22, no. 5, pp. 820–827, Sep. 1986.

[11] T. Noguchi, H. Tomiki, S. Kondo, and I. Takahashi, "Direct power control of PWM converter without power-source voltage sensors," *IEEE Trans. Ind. Appl.*, vol. 34, no. 3, pp. 473–479, May/Jun. 1998.

[12] J. Rodriguez *et al.*, "State of the art of finite control set model predictive control in power electronics," *IEEE Trans. Ind. Informat.*, vol. 9, no. 2, pp. 1003–1016, May 2013.

[13] Q. Chen, X. Luo, L. Zhang, and S. Quan, "Model predictive control for three-phase four-leg grid-tied inverters," *IEEE Access*, vol. 5, pp. 2834–2841, 2017.

[14] M. Ghanes, M. Trabelsi, H. Abu-Rub, and L. Ben-Brahim, "Robust adaptive observer-based model predictive control for multilevel flying capacitors inverter," *IEEE Trans. Ind. Electron.*, vol. 63, no. 12, pp. 7876–7886, Dec. 2016.

[15] B. Stellato, T. Geyer, and P. J. Goulart, "High-speed finite control set model predictive control for power electronics," *IEEE Trans. Power Electron.*, vol. 32, no. 5, pp. 4007–4020, May 2017.

[16] S. Vazquez, J. Rodriguez, M. Rivera, L. G. Franquelo, and M. Norambuena, "Model predictive control for power converters and drives: Advances and trends," *IEEE Trans. Ind. Electron.*, vol. 64, no. 2, pp. 935–947, Feb. 2017.

[17] Z. Zhang, F. Wang, T. Sun, J. Rodriguez, and R. Kennel, "FPGA based experimental investigation of a quasi-centralized DMPC scheme for a back-to-back converter," *IEEE Trans. Power Electron.*, vol. 31, no. 1, pp. 662–674, Jan. 2016.

[18] Z. Zhang, F. Wang, T. Sun, J. Rodriguez, and R. Kennel, "A computationally-efficient quasi-centralized DMPC for back-to-back converter PMSG wind turbine systems without dc-link tracking errors," *IEEE Trans. Ind. Electron.*, vol. 63, no. 10, pp. 6160–6171, Oct. 2016.

[19] S. M. N. Hasan and I. Husain, "A Luenberger-sliding mode observer for online parameter estimation and adaptation in high-performance induction motor drives," *IEEE Trans. Ind. Appl.*, vol. 45, no. 2, pp. 772–781, Mar. 2009.

[20] G. Feng, C. Lai, K. Mukherjee, and N. Kar, "Online PMSM magnet flux-linkage estimation for rotor magnet condition monitoring using measured speed harmonics," *IEEE Trans. Ind. Appl.*, vol. 53, no. 3, pp. 2786–2794, May–Jun. 2017.

[21] G. Feng, C. Lai, K. Mukherjee, and N. C. Kar, "Current injection-based online parameter and VSI nonlinearity estimation for PMSM drives using current and voltage dc components," *IEEE Trans. Transport. Electrific.*, vol. 2, no. 2, pp. 119–128, Jun. 2016.

[22] K. Liu and Z. Q. Zhu, "Position offset-based parameter estimation for permanent magnet synchronous machines under variable speed control," *IEEE Trans. Power Electron.*, vol. 30, no. 6, pp. 3438–3446, Jun. 2015.

[23] P. Antoniewicz and M. P. Kazmierkowski, "Virtual-flux-based predictive direct power control of ac/dc converters with online inductance estimation," *IEEE Trans. Ind. Electron.*, vol. 55, no. 12, pp. 4381–4390, Dec. 2008.

[24] M. Sumner, A. Abusorrah, D. Thomas, and P. Zanchetta, "Real time parameter estimation for power quality control and intelligent protection of grid-connected power electronic converters," *IEEE Trans. Smart Grid*, vol. 5, no. 4, pp. 1602–1607, Jul. 2014.

[25] E. Monmasson and M. N. Cirstea, "FPGA design methodology for industrial control systems: A review," *IEEE Trans. Ind. Electron.*, vol. 54, no. 4, pp. 1824–1842, Aug. 2007.

[26] L. Y. Pao and K. E. Johnson, "Control of wind turbines: Approaches, challenges, and recent developments," *IEEE Control Syst. Mag.*, vol. 31, no. 2, pp. 44–62, Apr. 2011.

[27] C. Huang, F. Li, and Z. Jin, "Maximum power point tracking strategy for large-scale wind generation systems considering wind turbine dynamics," *IEEE Trans. Ind. Electron.*, vol. 62, no. 4, pp. 2530–2539, Apr. 2015.

[28] Z. Zhang and R. Kennel, "FPGA based direct model predictive power and current control of 3L NPC active front ends," in *Proc. Int. Exhib. Conf. Power Electron., Intell. Motion, Renew. Energy Energy Manag.*, Nuremburg, Germany, May 2016, pp. 1–8.

[29] J. Holtz and N. Oikonomou, "Optimal control of a dual three-level inverter system for medium-voltage drives," *IEEE Trans. Ind. Appl.*, vol. 46, no. 3, pp. 1034–1041, May/Jun. 2010.

[30] S. Alepuz, S. Busquets-Monge, J. Bordonau, P. Cortes, J. Rodriguez, and R. Vargas, "Predictive current control of grid-connected neutral-point-clamped converters to meet low voltage ride-through requirements," in *Proc. IEEE Power Electron. Spec. Conf.*, 2008, pp. 2423–2428.

[31] R. C. Dorf and R. H. Bishop, *Modern Control Systems*, 10th ed. Upper Saddle River, NJ, USA: Prentice-Hall, 2000.

[32] *IEEE Standard Definition for the Measurement of Electric Power Quantities Under Sinusoidal, Nonsinusoidal, Balanced, or Unbalanced Conditions*, IEEE Standard 1459-2010 (redline version) (sponsored by the Power System Instrumentation and Measurements Committee) (Rev. Revision of IEEE Standard 1459-2000), 2010.

Zhenbin Zhang (S'13–M'16), was born in Shandong, China, in 1984. He received the B.S. degree in electrical engineering and automation from Harbin Engineering University, Harbin, China, in 2008, and the Ph.D. degree (*summa cum laude*) in electrical engineering from the Institute for Electrical Drive Systems and Power Electronics, Technical University of Munich, Munich, Germany, in 2016.

From 2008 to 2011, he studied control theory and engineering with Shandong University, Jinan, China. From 2016 to 2017, he was a Research Fellow and the team leader for the "Modern Control Strategies for Electrical Drives" Group with the Institute for Electrical Drive Systems and Power Electronics, Technische Universität München. Since 2017, he has been a Full Professor with Shandong University. His research interests include power electronics and electrical drives, sustainable energy systems, and smart grids.

Dr. Zhang was a recipient of the VDE Award, Suedbayern, Germany, in 2017.

Zhen Li was born in Shandong, China, in 1983. She received the master's degree in material science from the State Key Laboratory of Crystal Materials, Shandong University, Jinan, China, in 2004, and the Ph.D. degree in semiconductor materials from the Institute of Crystallography and Structural Physics, Friedrich-Alexander University Erlangen-Nürnberg (FAU), Erlangen, Germany, in 2017.

From 2014 to 2015, she was a Teaching and Research Assistant with FAU. Since 2018, she has been an Assistant Professor with Shandong Normal University, Jinan. Her research interests include defect detection of semiconductor materials, reliability of power electronics, and semiconductor devices.

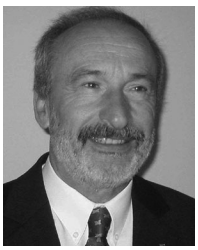

Marian P. Kazmierkowski (M'89–SM'91–F'98–LF'17) received the M.S., Ph.D., and Dr.Sci. degrees in electrical engineering from the Institute of Control and Industrial Electronics (ICIE), Warsaw University of Technology, Warsaw, Poland, in 1968, 1972, and 1981, respectively.

From 1987 to 2008, he was the Director of the ICIE. He has been the Head of the Centre of Excellence in Power Electronics and Intelligent Control for Energy Conservation, ICIE, since 2003. In 1974, he served a three-month internship at Siemens, Vienna, Austria, and in 1980–1984 he was with the RWTH Aachen as a Scholar of the Alexander von Humboldt Foundation. He is currently a Full Professor with the ICIE and a Consultant at the Electrotechnical Institute, Warsaw.

Dr. Kazmierkowski was the Vice President of the IEEE Industrial Electronics Society in 1999–2001 and the Editor-in-Chief of the IEEE TRANSACTIONS ON INDUSTRIAL ELECTRONICS in 2004–2006. He received an Honorary Doctorate degree from Aalborg University, Aalborg East, Denmark, in 2004, from the Institut National Polytechnique de Toulouse, Toulouse, France, in 2010, from the University of Zielona Góra, Zielona Góra, Poland, in 2012, and from the Bialystok University of Technology, Bialystok, Poland, in 2017. He was a recipient of the Dr.Ing. Eugene Mittelmann Achievement Award from the IEEE Industrial Electronics Society in 2005 and the SIEMENS Research Award in Poland in 2007. He was elected as the Corresponding (2007) and (2016) Full Member of the Polish Academy of Sciences and was the Dean of the Department of Engineering Sciences, Polish Academy of Sciences (2010–2014). He was recipient of the IEEE Medal in Power Engineering in 2017.

José Rodríguez (M'81–SM'94–F'10) received the Engineer degree in electrical engineering from the Universidad Técnica Federico Santa María, Valparaíso, Chile, in 1977, and the Dr.-Ing. degree in electrical engineering from the University of Erlangen, Erlangen, Germany, in 1985.

He has been with the Department of Electronics Engineering, Universidad Técnica Federico Santa María, since 1977. He is currently a Full Professor and the Rector of Universidad Andrés Bello, Santiago, Chile. His main research interests include multilevel inverters, new converter topologies, control of power converters, and adjustable-speed drives.

Dr. Rodríguez has been an Associate Editor for the IEEE TRANSACTIONS ON POWER ELECTRONICS and the IEEE TRANSACTIONS ON INDUSTRIAL ELECTRONICS since 2002. He was a recipient of the Best Paper Award from the IEEE INDUSTRIAL ELECTRONICS MAGAZINE in 2008, the Best Paper Award from the IEEE TRANSACTIONS ON POWER ELECTRONICS in 2010, and the Best Paper Award from the IEEE TRANSACTIONS ON INDUSTRIAL ELECTRONICS in 2007 and 2011. He is a member of the Chilean Academy of Engineering.

Ralph Kennel (M'89–SM'96) was born in Kaiserslautern, Germany, in 1955. He received the Diploma and Dr.-Ing. (Ph.D.) degrees in electrical engineering from the University of Kaiserslautern, Kaiserslautern, in 1979 and 1984, respectively.

From 1983 to 1999, he worked on several positions with Robert BOSCH GmbH, Gerlingen, Germany. Until 1997, he was responsible for the development of servo drives. From 1994 to 1999, he was a Visiting Professor with the University of Newcastle upon Tyne, Newcastle upon Tyne, U.K. From 1999 to 2008, he was a Professor for electrical machines and drives with Wuppertal University (Germany). Since 2008, he has been a Full Professor at the Institute for Electrical Drive systems and Power Electronics, Technische Universtät München, Munich, Germany. His main research interests include sensorless control of ac drives, predictive control of power electronics, and hardware-in-the-loop systems.

Dr. Kennel is a Fellow of the Institution of Electrical Engineers and a Chartered Engineer in the U.K. Within the IEEE, he is Treasurer of the Germany Section as well as ECCE Global Partnership Chair of the IEEE Power Electronics Society.